Journal of Cleaner Production 418 (2023) 138130

Contents lists available at ScienceDirect

Journal of Cleaner Production

journal homepage: www.elsevier.com/locate/jclepro

Thermal performance investigation of a novel medium-temperature pilot-scale latent heat storage system at different charging and discharging temperatures

Laiquan Lv [a], Shengyao Huang [a], Yang Zou [b], Xinyi Wang [b], Hao Zhou [a,*]

[a] State Key Laboratory of Clean Energy Utilization, Institute for Thermal Power Engineering, Zhejiang University, Hangzhou, 310027, PR China
[b] Shanghai Boiler Works Co, Ltd, Shanghai, 200000, China

ARTICLE INFO

Handling Editor: Panos Seferlis

Keywords:
Phase change materials
Shell-and-tube
Medium-temperature
Charging/discharging temperature
Latent heat storage

ABSTRACT

Large-capacity medium-temperature latent heat storage (LHS) systems have the potential to be extensively utilized for waste heat recovery and peak load shifting. However, the phase change behavior and mechanism of medium-temperature phase change materials (PCMs) in shell-and-tube LHS systems, as well as the impact of charging and discharging temperatures on the thermal performance, are still unclear. To address these issues and verify the reliability of the cylindrical pilot-scale LHS system, this article designed and constructed a novel cylindrical medium-temperature (up to 300 °C) LHS system with a large capacity (approximately 1 GJ) equipped with spiral and H-shaped fins. The research focused on investigating the impact of various charging and discharging temperatures on the thermal behavior of the LHS system to adapt different temperature scenarios in waste heat recovery while also analyzing the coupling effect of heat conduction and natural convection during charging and discharging and depicting the PCM liquidus based on thermocouple data. The experimental findings indicated that increasing the charging temperature could effectively shorten the charging duration, with a decrease from 5.99 h at 280 °C to 4.00 h at 300 °C, representing a reduction of 33.22%. In contrast, the impact of decreasing the discharging temperature on the discharging duration was less significant than that of increasing the charging temperature. Besides, the differences in heat transfer mechanisms between the charging and discharging processes were analyzed. In the charging process, the heat transfer was initially dominated by heat conduction, followed by natural convection. Conversely, heat conduction predominantly governed the heat transfer process in the discharging process. The heat transfer process dominated by heat conduction would increase the non-uniformity of PCM temperature on the horizontal plane, while the heat transfer process dominated by natural convection would alleviate this non-uniformity. Moreover, the accumulative stored energy under the charging temperature of 290 °C was 952.37 MJ, while the released energy under the discharging temperature of 160 °C was 648.72 MJ, which was approximately 10–200 times greater than those documented in existing studies.

1. Introduction

Thermal energy storage (TES) has been widely adopted in various fields to deal with the intermittency of renewable energy sources and to optimize energy consumption and peak load management (Alem Kebede et al., 2022; Chavan et al., 2022). One of the most promising forms of TES is latent heat storage (LHS), which stores energy through phase change processes. During the phase change of a material, typically a phase change material (PCM), energy is absorbed or released in LHS systems, which can be a solid-liquid or liquid-gas phase change. PCM-based TES systems have several advantages, including high energy density, low temperature variation, and storing energy at a constant temperature (Waseem et al., 2021; Zhou et al., 2022). These systems have a wide range of applications, including waste heat recovery (White and Sayma, 2020), heavy electronic equipment cooling (Rajesh Baby and Balaji, 2012; Lv et al., 2022), solar thermal energy storage (Zhou et al., 2021; Mosleh and Ahmadi, 2019), building temperature regulation (Jahangir Khan et al., 2020), air conditioning (Bourne and Novoselac, 2016), vapor absorption refrigeration system (Mumah, 2008), and medical application (Braxmeier et al., 2009).

Many important review articles have been published on LHS systems,

* Corresponding author.
E-mail address: zhouhao@zju.edu.cn (H. Zhou).

https://doi.org/10.1016/j.jclepro.2023.138130
Received 18 May 2023; Received in revised form 29 June 2023; Accepted 15 July 2023
Available online 16 July 2023

Nomenclature

Abbreviation

HETH	heat exchange tubes with H-shaped fins
HETS	heat exchange tubes with spiral fins
HTF	heat transfer fluid
LHS	latent heat storage
PCM	phase change material
TES	thermal energy storage

Symbol

c_p	specific heat (kJ/kg·K)
E	accumulative energy (kJ)
k	thermal conductivity (W/(m·K))
m	mass (kg)
P	power (kW)
Q	thermal energy (kJ)
T	temperature (°C)

Greek letter

ΔH	latent heat (kJ/kg)
μ	dynamic viscosity (mPa·s)
ρ	density (kg/m^3)
η	efficiency (%)
ΔW	uncertainty

Subscripts

1	before the charging/discharging process
2	after the charging/discharging process
c	charging
d	discharging
in	the HTF inflow of the heat exchange tube
l	liquid
m	melting
out	the HTF outflow of the heat exchange tube
s	solid
sf	solidification
tank	the PCM tank

including the selection of PCM (Tao and He, 2018; Agyenim et al., 2010), formulas for heat transfer and phase change problems (Marian Diaconu et al., 2023), studies on hybrid heat transfer enhancement (Mahdi et al., 2019; Khademi et al., 2022), energy and exergy performance assessments (Li, 2015), cascades of multiple PCMs (Lakshmi Narasimhan, 2019; Shen et al., 2022), geometric and design parameters (Ammar, 2018; Kalapala and Krishna Devanuri, 2018; Lv et al., 2023), and numerical investigation (Al-abidiSohif Bin Mat et al., 2013).

In recent years, various types of PCMs have been investigated for LHS applications, including organic, inorganic, and eutectic PCMs. Of these PCMs, organic PCMs with lower phase transition temperatures, such as paraffin (Avci and Yusuf Yazici, 2013; Joybari et al., 2019; Yang et al., 2020) and fatty acids (Zhang et al., 2020), in LHS systems have been widely studied. For example, Avci and Yusuf Yazici (2013) conducted an experimental study using paraffin as PCM filler in a horizontal shell-and-tube LHS system, which investigated the melting and solidification behavior of paraffin during the charging and discharging processes and the influence of inlet temperature on the processes. Moreover, fatty acids exhibit greater latent heat of fusion and demonstrate repeatable melting and solidification behavior compared to paraffin, with minimal undercooling. As a result, researchers have shown interest in their utilization within LHS systems. Zhang et al. (2020) introduced an innovative fractal-tree-shaped structure as the fin of a shell-and-tube LHS, utilizing lauric acid and water as PCM and HTF, and numerical research proved that the innovative fin decreased the charging and discharging duration of the LHS system by 66.2% and 4.4%. Yang et al. (2023) reported on a cascaded LHS system that used paraffin and erythritol as PCMs to recover waste heat. The experimental results showed that under charging conditions of 100 L/h and 160 L/h, the system could increase the waste heat recovery rate from 15.8% to 63.4%. Furthermore, the melting and solidification properties of salt hydrates (Lin et al., 2020a) and salts (Sodhi et al., 2019; Gurpreet Singh Sodhi and Muthukumar, 2021) in the LHS system have also been reported. Lin et al. (2020a) introduced a new type of pillow plate heat exchanger using sodium acetate trihydrate and water as PCM and HTF and investigated its charging and discharging performance, which demonstrated that the energy released by the new LHS system could reach 6.3 MJ at an average power of 4 kW. Sodhi et al., 2019 used sodium nitrate and air as PCM and HTF and improved the heat transfer rate during the charging process by modifying the cylindrical shell of the horizontal shell-and-tube LHS system to a conical shell using numerical research methods.

Besides, various configurations of LHS systems have been proposed, including shell-and-tube, plate, and finned-tube heat exchangers (Agyenim et al., 2010). Of these configurations, the finned-tube PCM heat exchanger has been widely investigated due to its high heat transfer performance and compact design (Mahdi et al., 2019). The fins increase the surface area and enhance the heat transfer between the PCM and the HTF, resulting in a higher heat transfer rate and more efficient energy storage and release. Liu et al. (2019) proposed two innovative longitudinal triangular fins with different layouts to improve the discharging performance of shell-and-tube LHS systems. The proposed triangular fins significantly improved the discharging performance of PCM and shortened the solidification time by 38.3% compared with traditional rectangular fins. Besides, Duan et al. (2020) and Zhang et al. (2022) also studied the strengthening effect of multi-helical fins and snowflake fins on charging and discharging performance based on numerical research and lab-scale single-tube experiments.

In addition to investigating different types of PCMs and heat exchanger configurations, scholars have also examined the impact of charging and discharging HTF temperatures on LHS system performance. Fadl and Eames (2019) designed and constructed a vertical multi-pipe LHS system to produce domestic hot water and studied the effects of varying charging and discharging temperatures on the transient temperature distribution, charging and discharging time, instantaneous power and cumulative energy. Their experimental results showed that increasing the temperature of charging HTF from 60 to 70 and 80 °C reduced the charging time by 3.5 and 5.5 h, respectively. Lin et al. (2020b) studied the performance of sebacic acid/expanded graphite composite material in a double helical coil heat exchanger and the effect of inlet HTF temperature on the performance of the LHS system. They found that as the HTF temperature increased from 160 to 200 °C, the charging time of the LHS system decreased from 333 to 135 min, a decrease of 59.46%. Gurpreet Singh Sodhi and Muthukumar (2021) examined the effects of charging and discharging air temperatures and flow rates on high-temperature LHS system performance. By increasing the charging HTF temperature from 340 to 360 and 380 °C, the charging duration of the LHS system was reduced from 485 to 354 and 296 min, respectively, representing a decrease of 27.01% and 38.97%. The temperature of the discharging HTF decreased from 265 to 245 and 225 °C, and the discharging duration was shortened from 608 to 428 and 336 min, respectively, representing a decrease of 29.61% and 44.74%.

The reviewed literature indicates that many studies have explored PCMs and LHS systems, the majority of them have focused on low-capacity systems for single HTF tubes at low temperatures, with only a

small portion dedicated to large-scale medium-temperature LHS systems. Besides, the phase change behavior and mechanism of medium-temperature PCMs in shell-and-tube LHS systems, as well as the impact of charging and discharging temperatures on thermal performance, are still not thoroughly studied. The significant thermal stress problem cannot be ignored in medium-temperature LHS systems, especially cubic LHS systems. Therefore, this article aimed to design and construct a pilot-scale shell-and-tube type LHS system with a large capacity (approximately 1 GJ) and a medium temperature range (up to 300 °C) equipped with spiral and H-shaped fins. The system utilized commercial molten salt as PCM and heat transfer oil as the HTF. The article investigated the evolution of temperature distribution in the PCM tank, instantaneous power, and cumulative energy with time under various charging and discharging temperatures and discussed the heat transfer enhancement mechanism of coupling heat conduction and natural convection in multiple heat exchange tubes equipped with spiral and H-shaped fins. Finally, the cycle efficiency of the large-capacity LHS system was calculated under different charging and discharging temperatures. The results obtained in this study provide important insights into the design and development of industrial-scale LHS systems and the determination of operating parameters, paving the way for the application of large-scale medium-temperature LHS systems.

2. Experimental setup and procedure

2.1. System description of the LHS system

To investigate the effect of various charging and discharging temperatures on the thermal performance of a pilot-scale LHS system, a medium-temperature LHS system equipped with heating and cooling systems was constructed at Zhejiang University. Fig. 1 illustrates the schematic diagram of the experimental system, which comprises four main components: a PCM storage tank, an HTF heating system, a water cooling system, and a data acquisition system. These components work together to ensure the effective operation of the LHS system and accurate data measurement.

The PCM tank is cylindrical, all welded from carbon steel, with a height, inner diameter, and thickness of 1450, 1530, and 20 mm, respectively, providing a volume of approximately 2.5 m^3. To facilitate medium-temperature PCM loading, two 325 mm diameter holes were cut into the lid that was welded onto the top of the PCM tank. Besides, 24 sleeves were welded for thermocouple positioning at 302, 910, and 1260 mm from the bottom of the tank, as shown in Fig. 2 (a). Furthermore, two sets of heat exchange tubes with spiral fins (HETS) and H-shaped fins (HETH), which are equivalent except for the type of fins used, were equipped on the left and right sides of the PCM tank. Each set of heat exchange tubes contains 125 tubes, and the turning of HTF in the tubes is achieved through the same U-shaped connecting tube. The heat exchange tubes have an outer diameter, inner diameter, and length of 32, 26, and 910 mm, with inlets and outlets all located above the tank. Detailed dimensions of the PCM tank and the heat exchange tubes are presented in Figs. 3 and 4.

The main equipment of the HTF heating system comprises an HTF boiler and a circulating HTF pump, where the HTF is circulated through the dynamic temperature control system provided by the boiler and the power provided by the pump to supply heat to the PCM during the charging process. This circuit includes three vortex flow sensors for measuring the volume flow rate and a series of valves to control the flow direction and flow rate of HTF. On the other hand, the water cooling system contains a water tank, a circulating water pump, and a heat exchanger, where high-temperature HTF transfers heat to low-temperature water in the heat exchanger to cool the HTF. The cooled HTF flows back to the boiler, which outputs the desired temperature through the dynamic temperature control system. The specifications of the experimental apparatus applied in the LHS system are summarized in Table 1.

Additionally, 42 K-type thermocouple probes were placed in the sleeves to monitor the temperature of the PCM inside the tank. Specifically, thermocouple sets #1, #2, and #3 are utilized to measure the temperature of the PCM in the upper, middle, and lower parts tank during the charging and discharging processes, with 6, 8, and 8 probes, respectively. Thermocouple sets #4 and #5 are applied to detect the PCM temperature at different heights near HETS and HETH. The exact installation locations of the thermocouples are marked in Fig. 3. Moreover, 4 additional thermocouple probes of the same specification are used to surveil the inlet and outlet HTF temperatures of HETS and HETH. The data collected by the thermocouple probes were recorded using an Agilent 34970A data acquisition system.

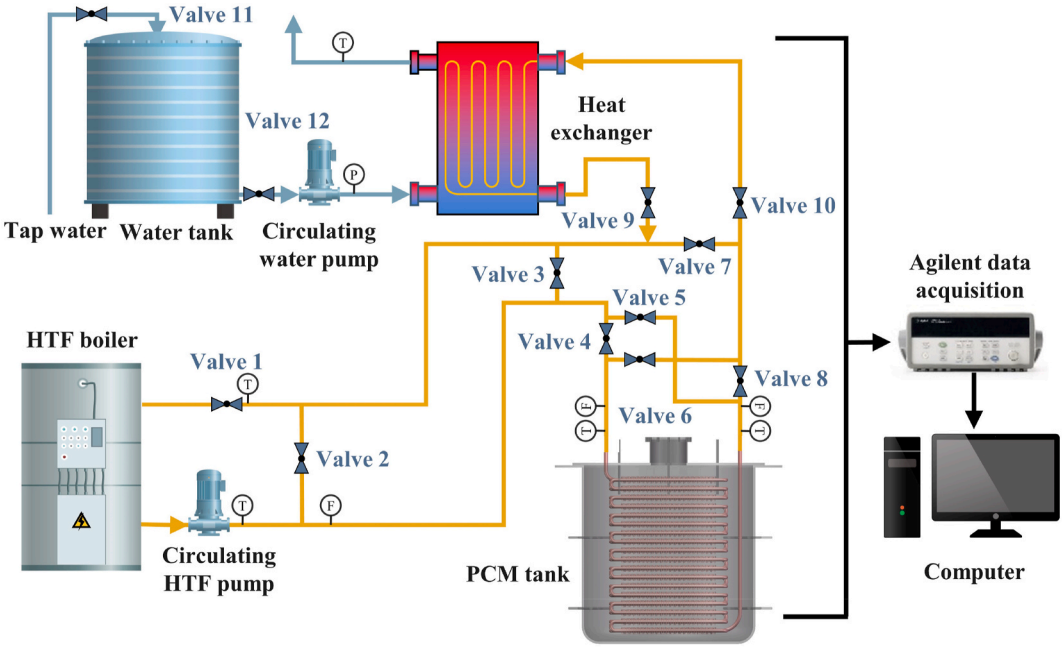

Fig. 1. Schematic illustration and main components of the experimental setup. (HTF flows from the left to the right in the PCM tank, achieving an up-down charging process, while HTF flows from the right to the left, realizing a down-up discharging process.)

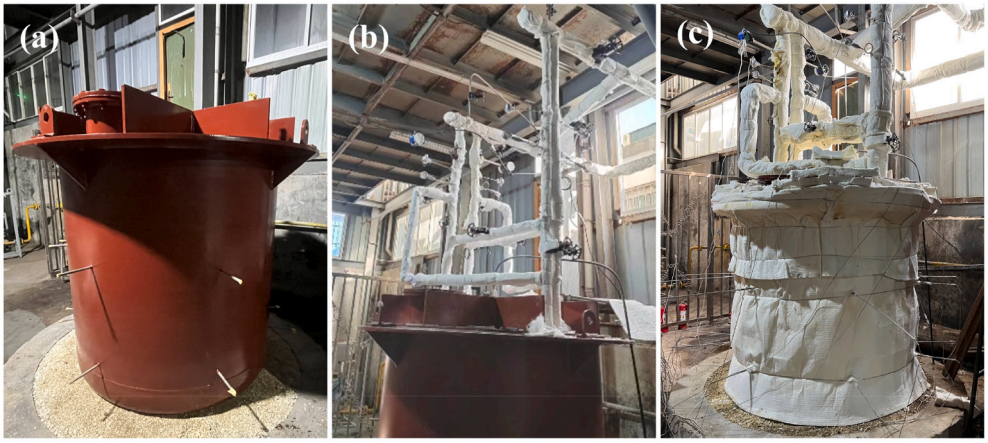

Fig. 2. Photographs of the PCM tank: (a) without tube connection, (b) with tube connection, and (c) with tube connection and aerogel insulation.

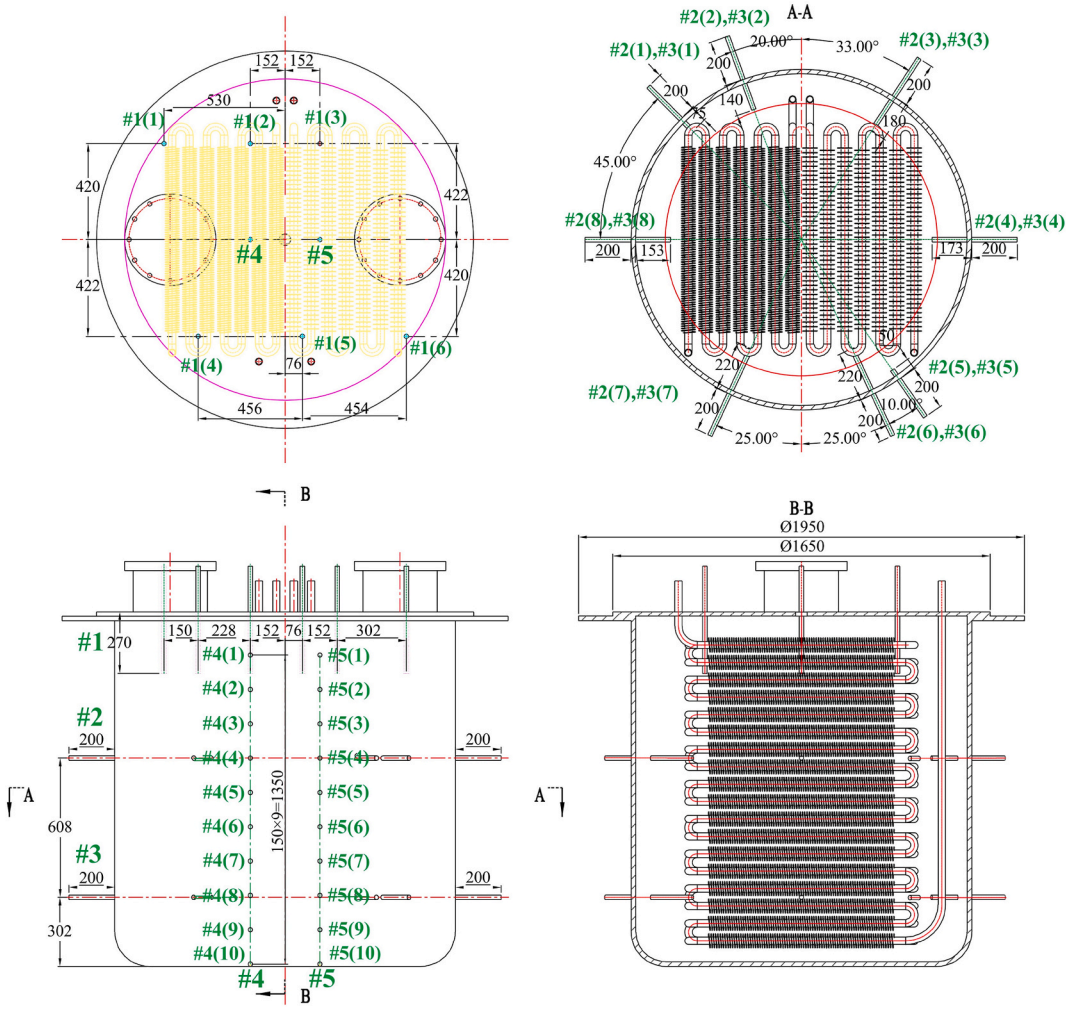

Fig. 3. Details regarding the dimensions of the PCM tank and thermocouples locations (unit: mm).

2.2. Key thermal properties of PCM, HTF, and carbon steel

The medium-temperature PCM used in this study was provided by HeatMate Technology (Shanghai) Co., Ltd. Its onset, peak, and offset temperatures during melting and solidification are 208.81, 225.35, 255.96 °C and 246.08, 219.90, 192.06 °C, respectively. Table 2 presents the essential thermal properties of the PCM, while the corresponding curves obtained by experimental characterization can be found in Fig. S1. In addition, the heat transfer oil (Therminol L-60) employed as HTF was purchased from Eastman Chemical Co., Ltd. The PCM tank and the two sets of heat exchange tubes were made of carbon steel from Shanghai Boiler Works Co., Ltd. Table 2 summarizes the thermal properties of the PCM, HTF, and carbon steel used in the experiments.

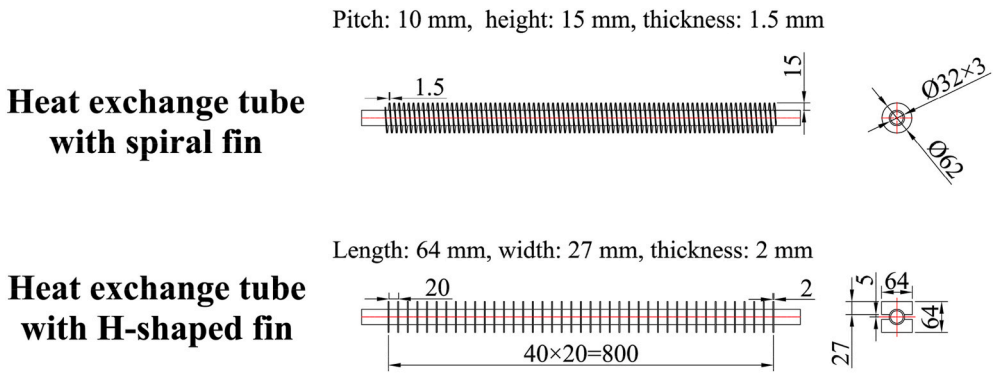

Fig. 4. Details regarding the dimensions of the heat exchange tubes with spiral and H-shaped fins (unit: mm).

Table 1
Specifications of the experimental apparatus applied in the LHS system.

Apparatus	Specifications
HTF boiler	YDW-225, maximum operating power: 225 kW
Thermocouple probes	Temperature range and error: 0–1100 °C and ±1 °C
Vortex flow sensors	LUGB-15C, flow range and error: 0–80 L/min and ±1.5%
Data acquisition instrument	Agilent 34970A

Table 2
Thermal properties of the PCM, HTF, and carbon steel (Lv et al., 2023).

Properties	Symbol	Units	PCM	HTF (200 °C/ 290 °C)	Carbon steel
Solidus/liquidus density	ρ_s/ρ_l	kg/m^3	2213.5/ 1924.6	868/792	7850
Peak melting/ solidification temperature	T_m/T_{sf}	°C	225.35/ 219.90	–	–
Latent heat	$\Delta H_m/\Delta H_{sf}$	kJ/kg	117.0/ 120.0	–	–
Specific heat	c_p	kJ/ (kg·K)	1.536	2.209/ 2.520	0.47
Thermal conductivity	k	W/ (m·K)	0.503	0.1079/ 0.096	48.85
Dynamic viscosity	μ	mPa·s	4.34	0.62/0.323	–

2.3. Experimental procedure

After the installation of the experimental setup was completed, the granular PCM provided by the supplier was filled into the PCM tank. Firstly, the operator opened the corresponding valves, started the boiler, and set the temperature of the dynamic temperature control system to 300 °C for heating the heat exchange tubes and air inside the PCM tank. Subsequently, the PCM was weighed and added to the tank through the loading holes. Due to the significant thermal resistance between the granular PCM and the heat exchange tube, it took 3 days to load 4130 kg of PCM to the PCM tank until the liquid PCM level covered the top fins of the heat exchange tube.

Before the charging and discharging experiments, the solid PCM inside the tank was preheated to approximately 190–195 °C to unify the initial temperature distribution and avoid thermal stress caused by significant volume changes of PCM. The average temperature of the PCM was determined by taking the mean of the temperatures recorded by 26 thermocouples, including #1(1, 2, 3, 4, 5, 6), #2(1, 3, 4, 6, 7, 8), #3(1, 3, 4, 6, 7, 8), #4(2, 4, 8, 10), and #5(2, 4, 8, 10). Valves 1, 4, 7, and 8 were opened, and the output HTF temperature was set to 210 °C to preheat the PCM from up to down. The preheating process was finished when the average temperature of the PCM increased to the desired value.

This article conducted three experiments under various charging/discharging temperatures (280/150, 290/160, and 300/170 °C) to obtain the effect of various charging/discharging temperatures on the thermal performance of the LHS system, as outlined in Table 3. Once the temperature of the PCM increased to 190–195 °C during preheating, valve 3 was opened, and the output HTF temperature was defined as a specific charging temperature, achieving external cyclic heating of the HTF without passing through the PCM tank. When the return HTF temperature, monitored by the dynamic temperature control system, reached the charging temperature, valve 3 was closed, and the HTF flow rate was adjusted to 15 L/min by valve 8 to start the charging process. The discharging process was implemented immediately when the temperature of PCM reached 265 °C, i.e., the end of the charging process. At the moment, valves 4, 7, and 8 were closed, while valves 1, 5, 6, 9, 10, 11, and 12 were kept open, and the output HTF temperature was modified to the corresponding discharging temperature. The HTF flow rate was adjusted to about 15 L/min by valve 6. The discharging process was considered complete once the temperature of PCM dropped to 190–195 °C. It is noteworthy that during the charging process, the PCM was charged from up to down to prevent the lower PCM from melting before the upper PCM, thereby avoiding compression of the liquid PCM with lower density and the formation of stress on the tank and heat exchange tube. Conversely, during the discharging process, the flow direction of the HTF was reversed to allow it to first contact the low-temperature PCM and then the high-temperature PCM, achieving temperature cascade utilization. The impact of up-down and down-up HTF flow during the discharging process on the thermal performance of LHS systems and the PCM phase change behavior will be explored in future research.

2.4. Schematic diagram of the PCM liquidus

To visually illustrate the melting and solidification processes of PCM during charging and discharging, a simplified representation of the PCM liquidus was performed based on data obtained from thermocouple probes. The peak melting temperature of PCM during both processes is approximately 225 °C, which was selected to determine the solid-liquid interface. Accordingly, when the temperature recorded by a thermocouple exceeds 225 °C, the nearby PCM is considered to be in the liquid

Table 3
Critical parameters used under different experimental cases.

Case number	Charging temperature (°C)	Discharging temperature (°C)	HTF flow rate in heat exchanger tubes (L/min)
1	280	150	15
2	290	160	15
3	300	170	15

state, while a temperature below 225 °C indicates the solid phase. For the sake of simplicity, the coexistence of solid and liquid phases during PCM melting and solidification was ignored in the construction of the PCM liquidus diagram. Additionally, experimental findings indicated that the heat transfer performance of HETS and HETH did not exhibit significant differences during the charging and discharging processes (Section 3), and the difference in PCM liquidus was not significant. Consequently, the PCM liquidus is believed to be symmetrical on both sides of the HETS and HETH configurations.

Furthermore, the determination of the PCM liquidus in the vertical direction primarily relied on thermocouple sets #4 and #5, while in the horizontal direction, it was determined by thermocouple sets #1, #2, and #3. However, it is essential to emphasize that during the charging and discharging processes, the melting and solidification of PCM initially occur near the tube wall and progressively diffuse outward. Therefore, this does not mean no liquid PCM is present in the solid phase portion of the PCM liquidus diagram.

2.5. System performance analysis

The instantaneous power (p) of TEHS and THEH can be obtained by applying equation (1), taking into account the temperature difference between the inlet and outlet temperatures and assuming negligible heat loss. The accumulative energy (E) is calculated by multiplying the power by the time, as illustrated in equation (2):

$$P = \dot{m} c_{p,\mathrm{HTF}} (T_{\mathrm{in}} - T_{\mathrm{out}}) \tag{1}$$

$$E = \int_0^t P \cdot \mathrm{d}t \tag{2}$$

where $\dot{m}$ and $c_{p,\mathrm{HTF}}$ refer to the mass flow rate and specific heat capacity of HTF, and T_{in} and T_{out} represent the inlet and outlet HTF temperatures.

Furthermore, the charging/discharging efficiency (η_c/η_d) and cycle efficiency (η) of the LHS system are determined using equations (3)–(5):

$$\eta_c = \frac{Q_{s,c} + Q_{l,c}}{E_c} = \frac{\left(m_{\mathrm{PCM}} \overline{c}_{p,\mathrm{PCM}} + m_{\mathrm{tank}} \overline{c}_{p,\mathrm{tank}}\right)\left(T_{2,c} - T_{1,c}\right) + m_{\mathrm{PCM}} \Delta H_m}{E_c} \tag{3}$$

$$\eta_d = \frac{E_d}{Q_{s,d} + Q_{l,d}} = \frac{E_d}{\left(m_{\mathrm{PCM}} \overline{c}_{p,\mathrm{PCM}} + m_{\mathrm{tank}} \overline{c}_{p,\mathrm{tank}}\right)\left(T_{2,d} - T_{1,d}\right) + m_{\mathrm{PCM}} \Delta H_s} \tag{4}$$

$$\eta = \frac{E_d}{E_c} \tag{5}$$

where the sensible, latent heat stored during charging is donated by $Q_{s,c}$ and $Q_{l,c}$, while that released during discharging is donated by $Q_{s,d}$ and $Q_{l,d}$, respectively. E_c and E_d represent the heat released and obtained by the HTF during charging and discharging, respectively. m_{PCM}, $c_{p,\mathrm{PCM}}$, m_{tank}, and $c_{p,\mathrm{tank}}$ refer to the mass and mean specific heat capacity of PCM and the PCM tank, respectively. Moreover, the temperatures of the PCM before and after charging are denoted by $T_{1,c}$ and $T_{2,c}$, respectively, while $T_{1,d}$ and $T_{2,d}$ represent those before and after discharging.

2.6. Uncertainty analysis

The uncertainty of the given parameters in this article is denoted by temperature and volume flow rate, which can be calculated using Kline-Mcclintock's method (Kline and Mcclintock, 1953). Assuming there are n independent variables y_1, y_2, y_3, …, and y_n in a parameter W, whose uncertainty ΔW can be determined by the uncertainty of these variables Δy_1, Δy_2, Δy_3, …, and Δy_n employing equation (6):

$$\Delta W = \sqrt{\left[\frac{\partial W}{\partial y_1}\Delta y_1\right]^2 + \left[\frac{\partial W}{\partial y_2}\Delta y_2\right]^2 + \left[\frac{\partial W}{\partial y_3}\Delta y_3\right]^2 + \ldots + \left[\frac{\partial W}{\partial y_n}\Delta y_n\right]^2} \tag{6}$$

The following equation can calculate the uncertainty of power, accumulative energy, and cycle efficiency.

$$\Delta W(P) = c_{p,HTF} \sqrt{((T_{\mathrm{in}} - T_{\mathrm{out}}) \times \Delta W(\dot{m}))^2 + (\dot{m} \times \Delta W(T_{\mathrm{in}}))^2 + (-\dot{m} \times \Delta W(T_{\mathrm{out}}))^2} \tag{7}$$

$$\Delta W(E) = c_{p,HTF} \times t \times \sqrt{((T_{\mathrm{in}} - T_{\mathrm{out}}) \times \Delta W(\dot{m}))^2 + (\dot{m} \times \Delta W(T_{\mathrm{in}}))^2 + (-\dot{m} \times \Delta W(T_{\mathrm{out}}))^2} \tag{8}$$

$$\Delta W(\eta) = \sqrt{\left(\frac{1}{E_c} \times \Delta W(E_d)\right)^2 + \left(-\frac{E_d}{E_c^2} \times \Delta W(E_c)\right)^2} \tag{9}$$

3. Results and discussion

3.1. Charging processes under different temperatures

The mean HTF volume flow rates flowing through HETS and HETH under the charging temperatures of 280, 290, and 300 °C were 15.18 and 15.05, 15.17 and 15.06, 15.22 and 15.13 L/min, respectively, as presented in Fig. 5 (a). Increasing the charging temperature resulted in a shorter charging duration, from 5.99 h at 280 °C to 4.54 h at 290 °C and 4.00 h at 300 °C, respectively, by 24.21% and 33.22%. Fig. 5 (b) depicts the inlet and outlet HTF temperature evolution curves of HETS and HETH over time under different charging temperatures. Under the charging temperatures of 280, 290, and 300 °C, the inlet HTF temperatures of HETS and HETH rapidly increased and approached approximately 270, 280, and 290 °C, respectively, which was 10 °C lower than the output HTF temperatures from the boiler. The temperature difference was caused by the significant heat dissipation losses resulting from the long distance between them. While the outlet HTF temperatures of HETS and HETH exhibited a similar temperature trend, rapidly increasing after charging and gradually slowing down till the end of charging. The outlet HTF temperature under the charging temperature of 300 °C was higher than that at a lower charging temperature, but the temperature difference was smaller than that between the inlet temperatures, indicating that a higher HTF temperature could transfer more heat to the PCM. Moreover, the outlet temperature of HETS was lower than that of HETH, indicating that HETS could transfer heat faster to PCM and possessed better heat transfer performance.

3.1.1. Temperature analysis of thermocouple set #1 during charging processes

Thermocouple set #1, located 1260 mm from the bottom of the PCM tank, showed a fast temperature response because the high-temperature HTF first transferred heat through thermal conduction to the nearby PCM. Fig. 5 (c, d) present the temperature evolution curves of thermocouples #1(1–6) over time under different charging temperatures. In the early charging stage, thermocouple set #1 first demonstrated a slow temperature increase, suggesting entering the solid-liquid phase transition temperature zone of PCM. The temperature difference of thermocouple set #1 under different charging temperatures was small, possibly because the heat of the high-temperature HTF could not be transferred

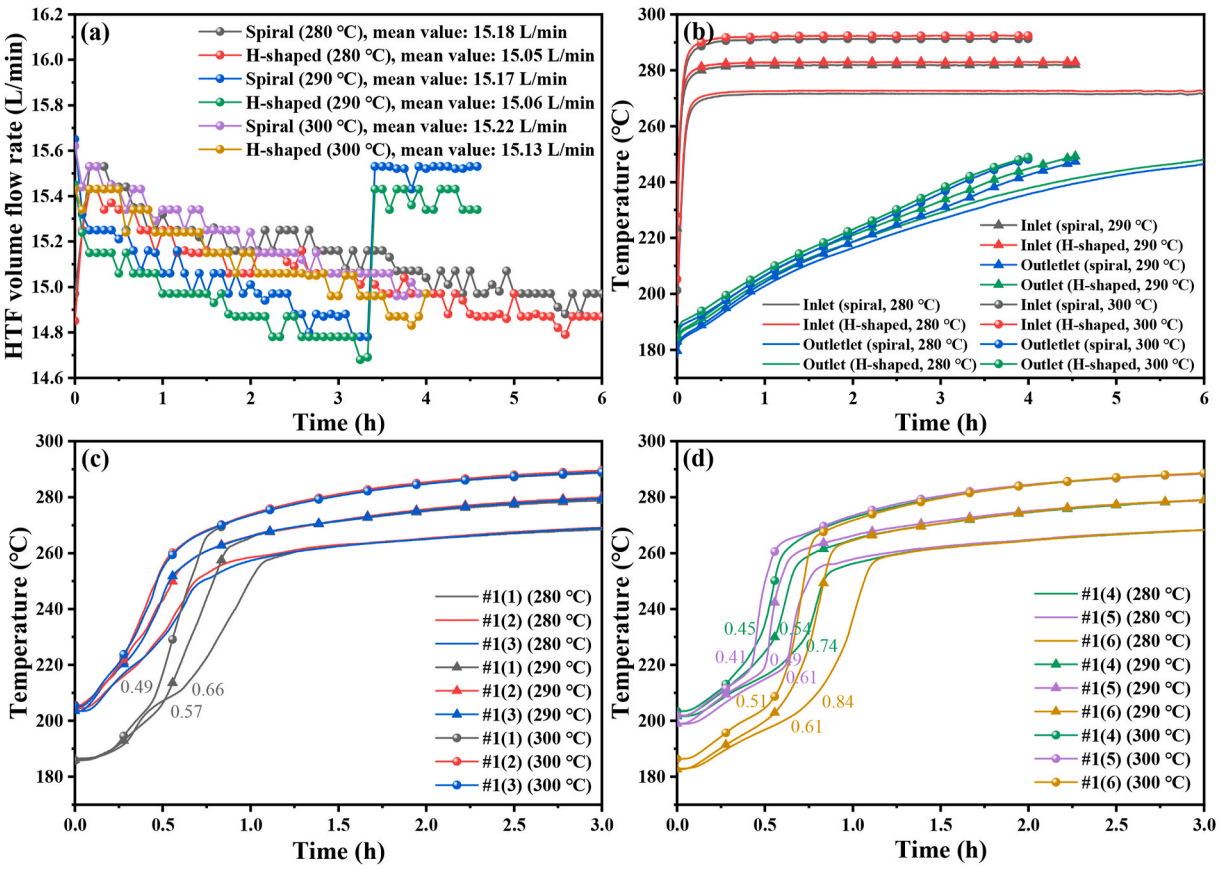

Fig. 5. Evolution of (a) HTF volume flow rates, (b) inlet and outlet temperatures of HETS and HETH, (c) thermocouples #1(1–3), and (d) thermocouples #1(4–6) over time under the charging temperatures of 280, 290, and 300 °C.

to PCM quickly by thermal conduction. As the charging process progressed, the PCM near the thermocouples melted gradually, and its temperature rapidly increased to a temperature close to HTF, corresponding to the liquid sensible heat zone of PCM. The temperature difference of thermocouple set #1 under different charging temperatures increased significantly after entering the liquid sensible heat zone of PCM, possibly due to the enhanced heat transfer caused by natural convection. After about 1 h of charging, the temperature difference between thermocouple set #1 gradually stabilized at about 10 °C under different charging temperatures, corresponding to the charging temperature difference of 10 °C.

3.1.2. Temperature analysis of thermocouple sets #2 and #3 during charging processes

Fig. 6 displays the temperature evolution of thermocouple sets #2 and #3, situated 910 and 302 mm from the bottom of the PCM tank, under varying charging temperatures. During the initial charging stage, similar to thermocouple set #1, the temperature difference of set #2 under different charging temperatures was slight. As the PCM near the thermocouples entered the liquid sensible heat zone, the temperature difference significantly increased and stabilized. This suggested that raising the charging temperature from 280 to 290 °C provided a greater driving force for transferring heat from the HTF to the PCM, shortening the charging duration. However, further raising the charging temperature to 300 °C had less impact on the charging duration because further increasing the charging temperature cannot increase the heat transfer flow rate in the same proportion. The poor thermal conductivity of the PCM affected the increase of heat transfer flow rate, which was manifested by higher outlet HTF temperature at higher charging temperature (Fig. 5 (b)).

Thermocouples #3(1, 3, 6, 7) exhibited a similar trend to set #2, while #3(2, 4, 5, 8) did not reach the PCM transition temperature at the end of charging, indicating that the PCM nearby did not completely melt.

3.1.3. Temperature analysis of PCM during charging processes

The temperature evolution of thermocouple sets #4 and #5, which are uniformly distributed in the vertical direction of the PCM tank under the charging temperature of 280 °C, is presented in Fig. 7 (a). The temperatures of thermocouple sets #4 and #5 increased from up to down due to the up-down charging process. Initially, the temperatures increased rapidly, indicating the solid sensible heat zone of PCM (190–220 °C). As charging progressed, the temperatures entered the platform zone, corresponding to the solid-liquid phase transition zone of PCM (220–230 °C), and maintained a slow temperature increase rate. Subsequently, as the PCM near the thermocouples completely melted, the temperatures rapidly increased again and eventually slowly approached the temperature of the nearby HTF, which corresponded to the liquid sensible heat zone of the PCM (230–290 °C). It is worth noting that the temperature increase rate in the liquid sensible heat zone was significantly higher than that in the solid sensible heat zone. This could be attributed to the natural convection caused by the liquid PCM, which strengthened the heat transfer between HTF and PCM. Fig. 7 (b) shows the temperature evolution curves of thermocouples #4(3, 6, 9) and #5 (3, 6, 9) under the charging temperatures of 280, 290, and 300 °C.

In addition, Fig. 7 (c, d) illustrate the average temperature curves of thermocouple sets #1, #2, and #3 and the PCM in the tank under different charging temperatures. The average temperature trends of thermocouple sets #1 and #2 were similar to those discussed in Sections 3.1.1 and 3.1.2, entering the liquid sensible zone of the PCM at approximately 0.5 and 2 h, respectively. The temperature difference was not significant under different charging temperatures but gradually

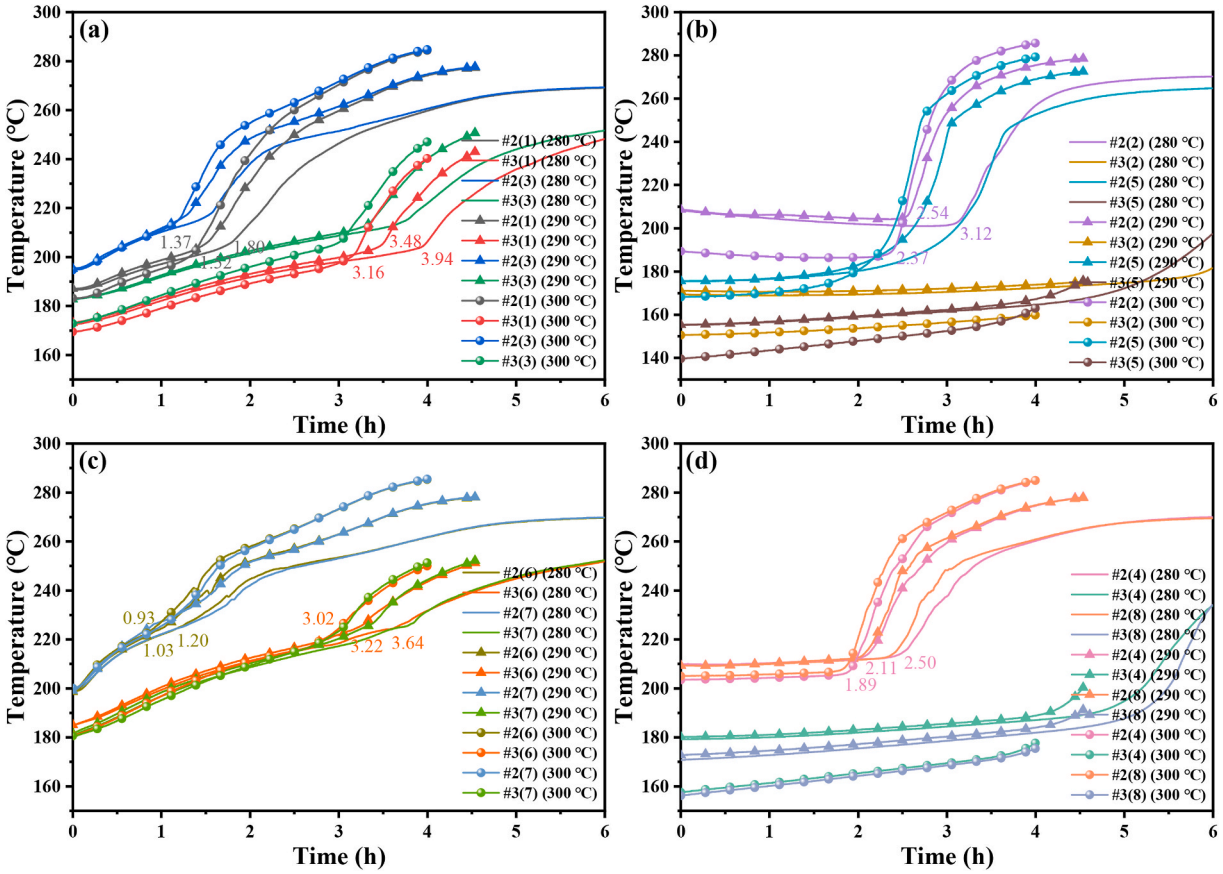

Fig. 6. Temperature evolution of (a) thermocouples #2(1, 3) and #3(1, 3), (b) #2(2, 5) and #3(2, 5), (c) #2(6, 7) and #3(6, 7), and (d) #2(4, 8) and #3(4, 8) over time under the charging temperatures of 280, 290, and 300 °C.

increased as the temperatures of the thermocouples entered the liquid sensible zone of the PCM. The average temperature of PCM first rapidly increased, followed by a turning point around 225 °C, then increased steadily. This was because the significant temperature difference between HTF and PCM during the initial charging stage increased the heat transfer rate. As the charging proceeded, the PCM near the heat exchange tube wall and fins gradually melted into the solid-liquid phase transition zone, leading to the emergence of a turning point. As the PCM near the wall became liquid, natural convection further strengthened heat transfer, so the temperature increase rate of the PCM was stable until the end of charging. Furthermore, increasing the charging temperature from 280 °C to 290 °C resulted in a higher temperature of the PCM within the same time, but continuing to increase the charging temperature to 300 °C had a limited effect.

Fig. 8 displays schematic diagrams of the PCM liquidus under different charging temperatures over time. The PCM liquidus initially scurried downward within the first 3 h, but its descent significantly slowed during the last 3 h. Two main factors contributed to this slowdown. Firstly, due to the temperature difference between the high-temperature HTF and upper PCM, the upper PCM melted quickly, but as the HTF temperature gradually decreased during the flow process, slowing down the melting rate of the lower PCM. Secondly, the natural convection caused by the formation of liquid PCM strengthened the heat transfer between HTF and PCM, accelerating the melting of PCM. The heat transfer of the PCM on the outer wall and bottom of the tank was achieved through thermal conduction, which was hindered by poor PCM thermal conductivity. Moreover, by increasing the charging temperature from 280 to 290 and 300 °C, a larger temperature difference between HTF and PCM enhanced heat transfer and increased the melting rate of PCM. After completing charging, the PCM liquidus with the charging temperature of 280 °C was lower near the outer wall of the TES unit, indicating more PCM melting, which may be due to the longer charging duration.

3.1.4. Charging performance

The instantaneous power of HETS and HETH increased rapidly to 39.51 and 38.86, 43.81 and 43.16, 47.35 and 47.12 kW after charging, respectively, under the charging temperatures of 280, 290 and 300 °C, and then gradually decreased until the end of charging, as plotted in Fig. 9 (a). The instantaneous power of HETS was always greater than that of HETH throughout the charging processes, further proving that HETS has better heat transfer performance than HETH during the charging process. Besides, increasing the charging temperature from 280 to 290 and 390 °C could increase the average power of both HETS and HETH from 45.2 ± 0.96 to 58.12 ± 0.97 and 67.62 ± 0.98 kW, respectively, by 28.58% and 49.60% (Fig. 9 (b)). The accumulative stored energy and charging efficiency of both HETS and HETH under the charging temperatures of 280, 290, and 300 °C were 977.84 ± 20.78, 952.37 ± 15.81, and 973.44 ± 14.07 MJ, 89.48%, 91.88%, and 89.61%, respectively, as depicted in Fig. 9 (c, d). The differences in accumulated energy and charging efficiency under different charging temperatures were 2.60% and 2.61%, proving the reliability of the experiments.

3.2. Discharging processes under different temperatures

The mean HTF rates through HETS and HETH under the discharging temperatures of 170, 160, and 150 °C were 14.12 and 14.17, 14.85 and 14.18, 14.01 and 13.95 L/min, respectively, as plotted in Fig. 10 (a). Decreasing the discharging temperature resulted in a shorter discharging duration, from 3.80 h at 170 °C to 3.18 h at 160 °C and 3.03 h at 150 °C, respectively, by 16.32% and 20.26%. Fig. 10 (b) illustrates the inlet and outlet HTF temperature curves of HETS and HETH under

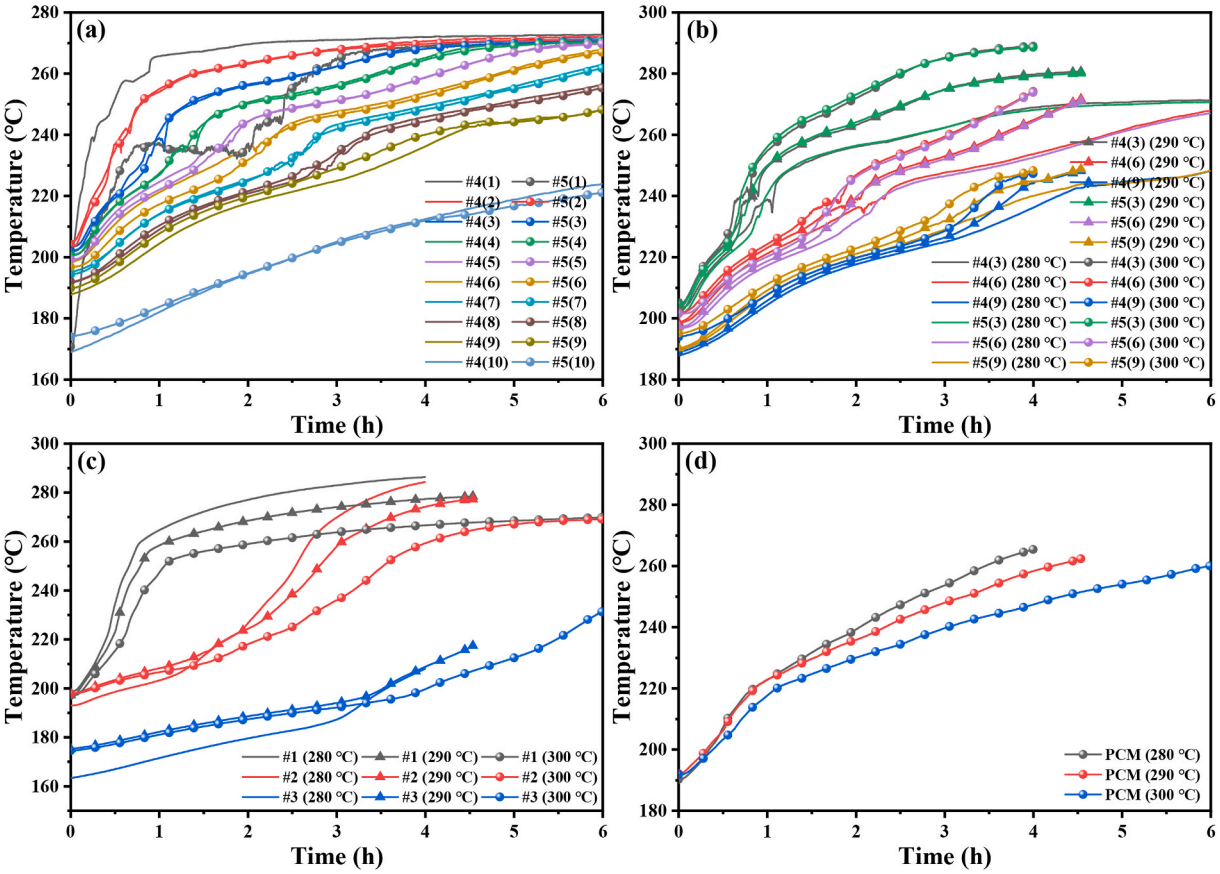

Fig. 7. Temperature evolution of (a) thermocouple sets #4 and #5 over time under the charging temperature of 280 °C, and (b) thermocouples #4(3, 6, 9) and #5(3, 6, 9), (c) thermocouple sets #1, #2, and #3, (d) PCM over time under the charging temperatures of 280, 290, and 300 °C.

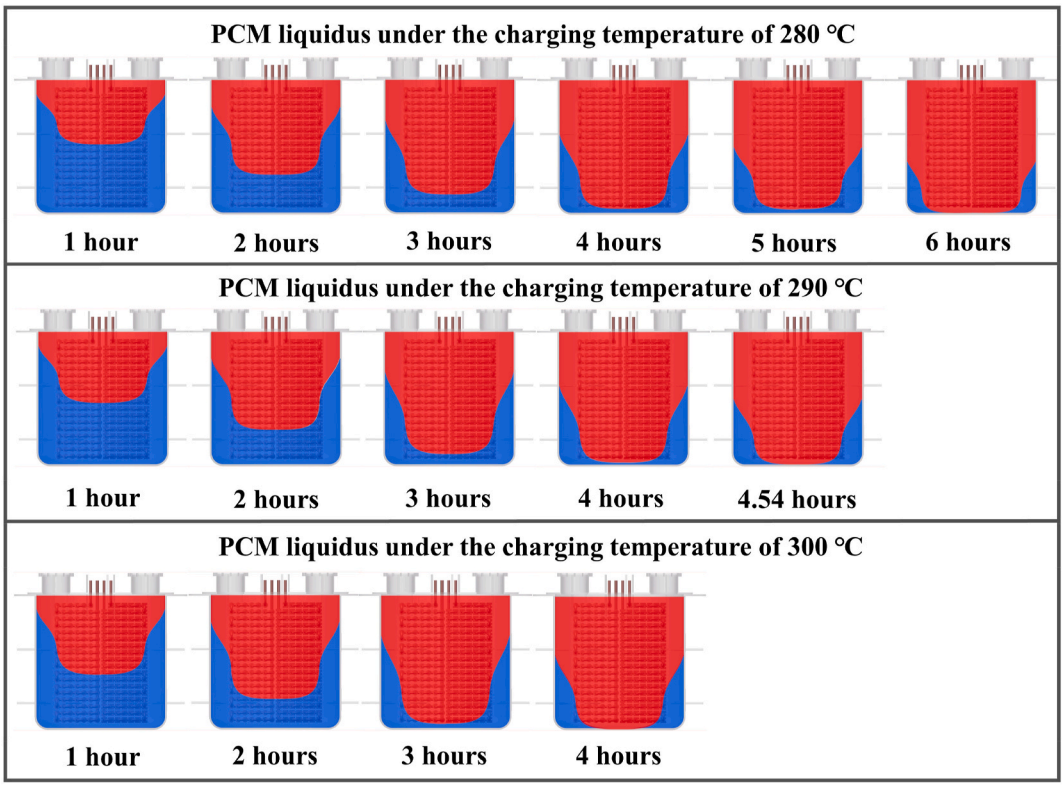

Fig. 8. Schematic diagrams of the PCM liquidus change under the charging temperatures of 280, 290, and 300 °C.

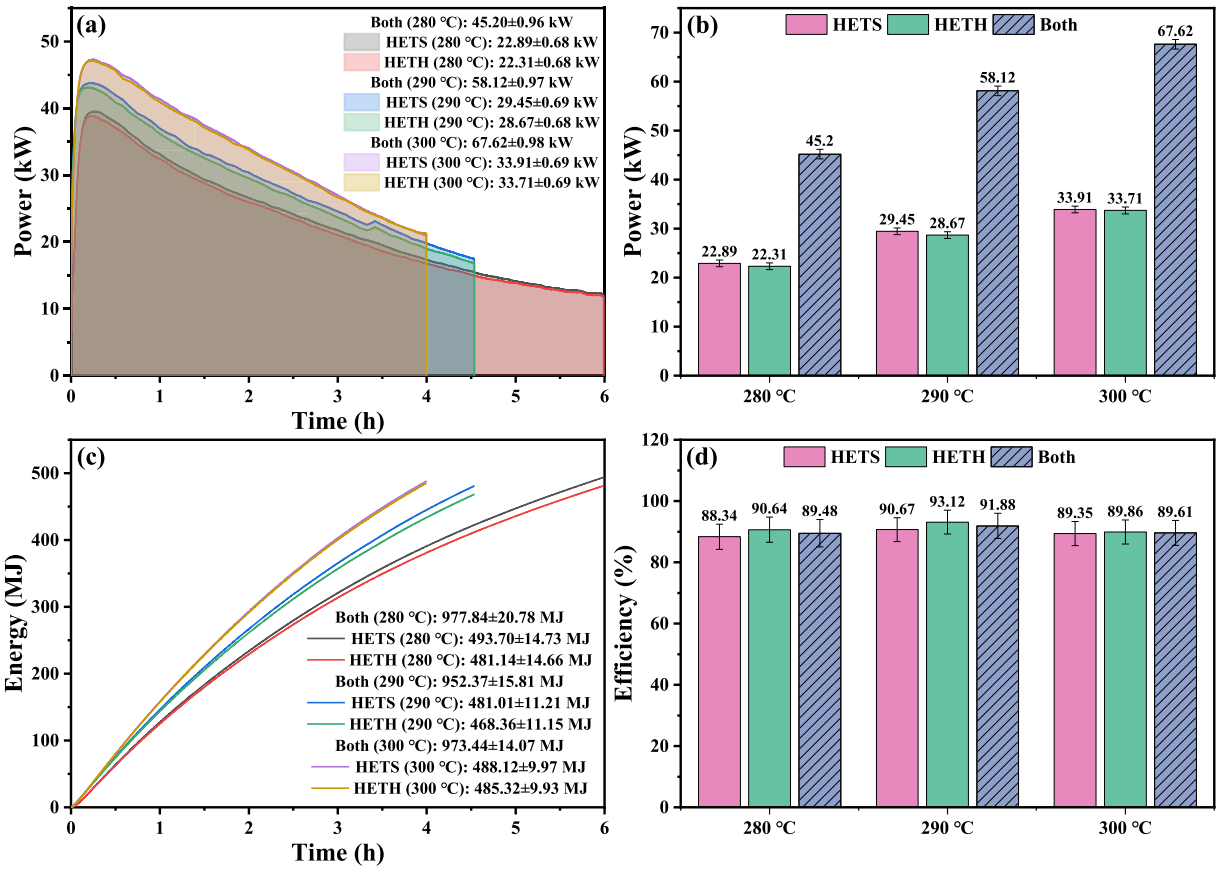

Fig. 9. (a) Instantaneous power curves, (b) average power of HETS, HETH, and both, (c) accumulative energy curves, and (d) charging efficiency of HETS, HETH, and both under the charging temperatures of 280, 290, and 300 °C.

different discharging temperatures. After the discharging began, the inlet temperature rapidly decreased after being cooled by water and then gradually approached the set temperature and remained unchanged. Under the discharging temperatures of 170, 160, and 150 °C, the outlet temperatures of HETS and HETH gradually decreased from approximately 285, 275, and 265 °C until the discharging processes ended. The reason for the difference in outlet temperatures was that the initial temperature distribution in the discharging processes was different. In addition, HETH possessed a higher outlet HTF temperature than HETS, indicating that HETH had better heat transfer performance during the discharging process, opposite to the charging process.

3.2.1. Temperature analysis of thermocouple set #1 during discharging processes

Thermocouple set #1 exhibited similar temperature trends under different discharging temperatures, as shown in Fig. 10 (c, d). Under the discharging temperatures of 170, 160, and 150 °C, thermocouple set #1 decreased at a low rate from approximately 290, 280, and 270 °C, respectively, followed by a gradual acceleration of the decrease rate, indicating that the PCM experienced the liquid sensible heat zone (290-230 °C). The main reason for the temperature drop rate change of thermocouple set #1 during the initial discharging process was the heat transfer change caused by PCM solidification near the heat exchange tube. The lower PCM could provide sufficient heat through thermal conduction and natural convection to low-temperature HTF in the early discharging stages. As the PCM solidified near the lower pipe wall, heat conduction dominated the heat transfer process, and the upper liquid PCM needed to provide more heat, thereby accelerating the temperature drop. After about 1.5 h of discharging, the temperatures of thermocouple set #1 remained unchanged at approximately 225 °C, suggesting that the nearby PCM entered the liquid-solid phase transition zone (230-220 °C). Subsequently, after the complete solidification of PCM, their temperatures decreased again, corresponding to the solid-state sensible heat zone (220-190 °C) of PCM. It is important to note that the temperature difference between thermocouple set #1 decreased in the initial discharging stage under various discharging temperatures, followed by stability in the liquid-solid phase transition zone, and then increased again in the later discharging stage.

3.2.2. Temperature analysis of thermocouple sets #2 and #3 during discharging processes

The temperature evolution curves of thermocouples sets #2 and #3 under different discharging temperatures are shown in Fig. 11. In the early discharging stage, thermocouple set #2 exhibited similar temperature change behavior under different discharging temperatures, whose temperatures rapidly decreased after discharging until approached phase change temperature. After approximately 1 h of discharging, the temperatures of thermocouples #2(1, 3, 6, 7) continued to decrease, indicating that the nearby PCM had solidified entirely. The thermocouple with a lower discharging temperature had a faster temperature decrease rate. While the temperatures of thermocouples #2(2, 4, 5, 8) exhibited almost the same behavior at different discharging temperatures, maintaining around 225 °C, indicating that the PCM near it was still in the liquid-solid phase transition zone.

The temperature curves of thermocouples #3(1, 3, 6, 7) near the PCM that melted during the charging process were similar to those of thermocouples #2(1, 3, 6, 7). Only an inconspicuous difference in the later discharging stage was observed under different discharging temperatures. While the temperatures of thermocouples #3(2, 4, 5, 8) near the unmelted PCM only slightly decreased or even increased.

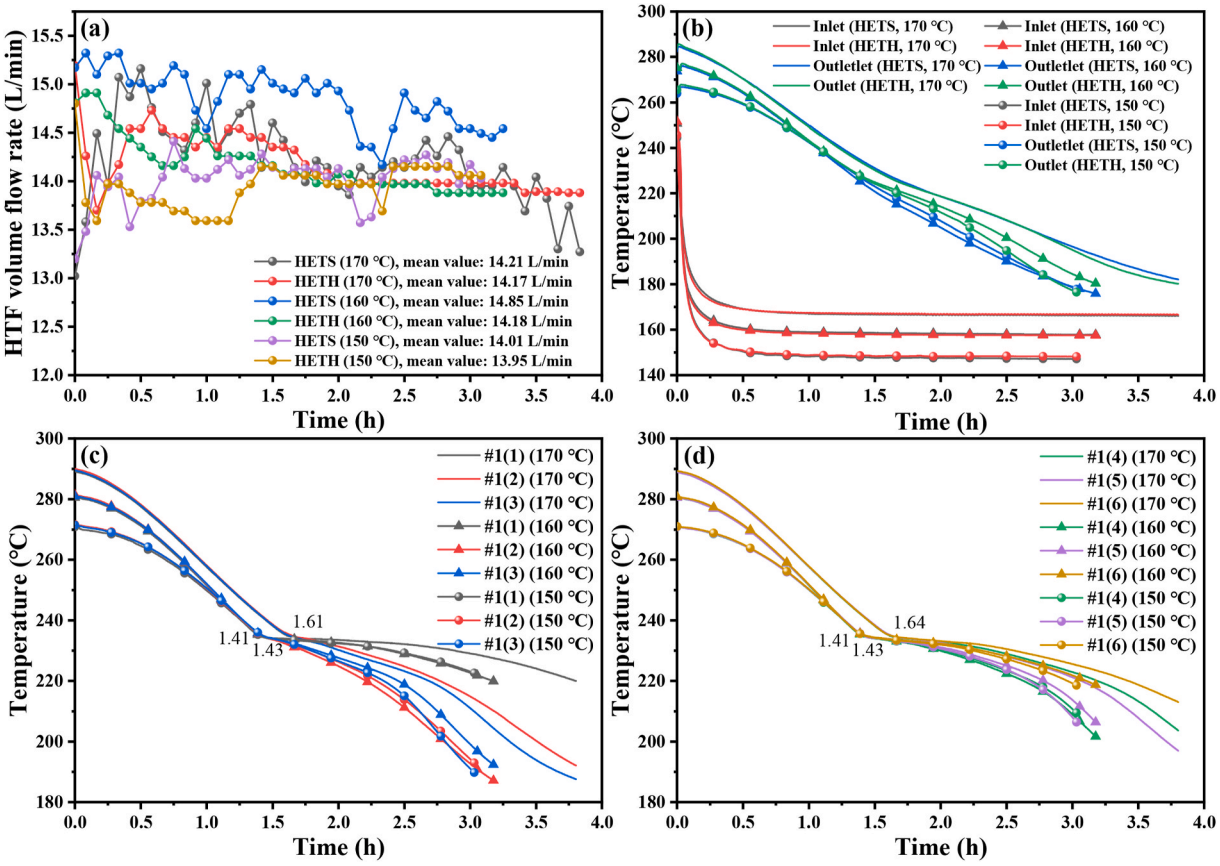

Fig. 10. Evolution of (a) HTF volume flow rates, (b) inlet and outlet temperatures of HETS and HETH, (c) thermocouples #1(1–3), and (d) thermocouples #1(4–6) over time under the discharging temperatures of 170, 160, and 150 °C.

3.2.3. *Temperature analysis of PCM during discharging processes*

Fig. 12 (a) presents the temperature evolution curves of thermocouple sets #4 and #5 over time under the discharging temperature of 170 °C. The temperatures of thermocouple sets #4 and #5 decreased from down to up due to the down-up discharging process. During the discharging process, three typical PCM zones were observed, namely the liquid sensible heat zone (290-230 °C), the liquid-solid phase transition zone (230-220 °C), and the solid sensible heat zone (220-190 °C). Unlike the charging process, the temperature decrease rate was higher in the liquid sensible heat zone during discharging than in the solid sensible heat zone. This could be attributed to the solidification of the liquid PCM near the heat exchange tube, which led to heat transfer between HTF and PCM through thermal conduction. As discharging progressed, the temperature of HTF gradually approached that of PCM, resulting in a slower temperature decrease rate in PCM. Fig. 12 (b) shows the temperature evolution curves of thermocouples #4(3, 6, 9) and #5(3, 6, 9) under the discharging temperatures of 170, 160, and 150 °C.

The temperature curves of thermocouple sets #1, #2, #3, and PCM in the tank under different discharging temperatures are illustrated in Fig. 12 (c, d). The temperatures of thermocouple sets #1 and #2 entered the liquid-solid phase transition zone of PCM at approximately 1.5 and 0.9 h, respectively, as discussed in Sections 3.2.1 and 3.2.2. Moreover, the temperature of the PCM first decreased rapidly, followed by a turning point around approximately 215 °C, and then continued to decrease. Lowering the discharging temperature from 170 °C to 160 °C resulted in a more significant temperature decrease in the PCM within the same time, but further lowering the discharging temperature to 150 °C had an insignificant impact. In addition, it should be noted that the impact of lowering the discharging temperature on the PCM temperature was smaller compared to increasing the charging temperature. This could be attributed to the natural convection involved during the charging process, while thermal conduction dominated the discharging process.

The schematic diagram of the PCM liquidus over time under different discharging temperatures is depicted in Fig. 13. The movement speed of the PCM liquidus near the heat exchange tube gradually decreased during the discharging process due to the gradually decreasing temperature difference between HTF and PCM. The upper PCM near the outer wall of the PCM tank remained in the liquid phase throughout the discharging process because the heat was difficult to transfer to the HTF through thermal conduction. Furthermore, lowering the discharging temperature accelerated the solidification rate of the PCM, but the effect was smaller than that of increasing the charging temperature to accelerate the melting rate of the PCM. This was consistent with the temperature results of the PCM during the charging and discharging processes.

3.2.4. *Discharging performance*

Fig. 14 (a) depicts the instantaneous power curves of HETS and HETH under the discharging temperatures of 170, 160 and 150 °C. Similar to the charging processes, the instantaneous power of HETS and HETH increased quickly to about 45–50 kW, followed by a gradual drop till the end of discharging. Decreasing the discharging temperature from 170 to 160 and 150 °C improved the average power of both from 49.46 ± 0.84 to 56.70 ± 0.87 and 61.69 ± 0.83 kW, respectively, by 14.64% and 24.73% (Fig. 14 (b)). Decreasing the discharging temperature increased the average power by about half that of increasing the charging temperature, consistent with the PCM temperature results discussed in Sections 3.1.3 and 3.2.3. The accumulative released energy and discharging efficiency of both HETS and HETH under the discharging temperatures of 170, 160, and 150 °C were 677.27 ± 11.57, 648.72 ± 9.94, and 673.73 ± 9.08 MJ, 84.16%, 80.61%, and 83.72%, respectively, with differences of 4.22% and 4.21%, as depicted in Fig. 14 (c, d).

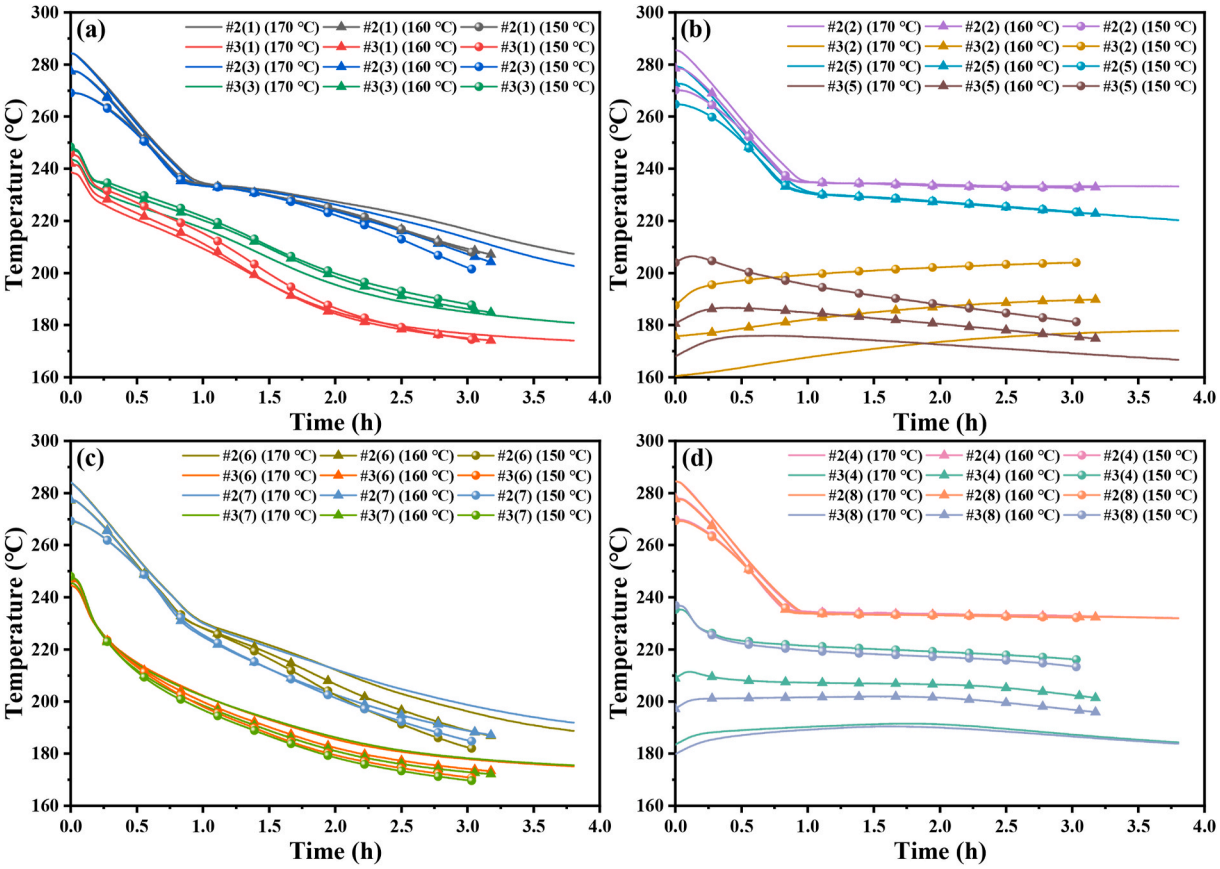

Fig. 11. Temperature evolution of (a) thermocouples #2(1, 3) and #3(1, 3), (b) #2(2, 5) and #3(2, 5), (c) #2(6, 7) and #3(6, 7), and (d) #2(4, 8) and #3(4, 8) over time under the discharging temperatures of 170, 160, and 150 °C.

3.3. System performance analysis

The cycle efficiency of the LHS system in cases 1, 2, and 3, calculated according to equation (5), were 69.11 ± 1.74%, 68.33 ± 1.55%, and 69.57 ± 1.56%, respectively. The efficiency of the three experiments was about 69%, which was obtained neglecting the upper liquid PCM near the outer wall of the PCM tank after discharging, and the actual value may be higher. Besides, the similar efficiency of the three experiments suggested that the cycle efficiency of the system was independent of the charging and discharging temperatures.

Table 4 compares the key parameters of the LHS systems for this work with those reported in previous studies. In comparison to previously reported LHS systems, the LHS system investigated in this study demonstrated a significantly higher TES capacity, approximately 10–200 times greater than those documented in existing studies listed in Table 4. The employed PCM exhibited an appealing melting temperature. Furthermore, the charging and discharging duration of the LHS system in this research was relatively short, allowing for rapid absorption of excess heat energy and providing larger power output in practical applications, such as waste heat recovery and peak load shifting. Regrettably, the cycle efficiency of the medium-temperature LHS system was inferior to that of the low-temperature LHS system. This discrepancy primarily arouse from higher temperatures leading to greater heat dissipation losses. Therefore, improving insulation performance is essential for LHS systems to achieve higher efficiency in practical applications. This study provides practical guidance and valuable insights for the industrial application of waste heat recovery and peak load shifting.

3.4. Limitation of this work

Some limitations in this study require further improvement in future research. Firstly, the insulation performance of the LHS system should be enhanced, as it is a primary contributor to the decrease in cycle efficiency. Secondly, incomplete melting or solidification of the PCM near the wall after charging or discharging can adversely affect cycle efficiency. Therefore, it is necessary to refine the design of the PCM tank to ensure a complete phase change. Thirdly, the working temperature range of the heat transfer oil used in the experiments is limited, which restricts the ability to conduct charging and discharging tests across a wider temperature range. Future research should explore using HTF with broader working temperature ranges to obtain more generalized results.

4. Conclusions

To obtain the phase transition behavior and mechanism of medium-temperature PCMs in shell-and-tube LHS systems, as well as the impact of charging and discharging temperatures on thermal performance, and to verify the reliability of cylindrical LHS systems, this study presented a novel cylindrical pilot-scale LHS system with spiral and H-shaped fins based on previous work. The research focused on investigating the impact of various charging and discharging temperatures on the thermal behavior of the LHS system, including charging and discharging duration, temperature profiles, instantaneous power, accumulative stored and released heat, and efficiency. Additionally, the study depicted the PCM liquidus during the charging and discharging processes based on thermocouple data and analyzed the effects of heat conduction and natural convection. The conclusions could be drawn as follows:

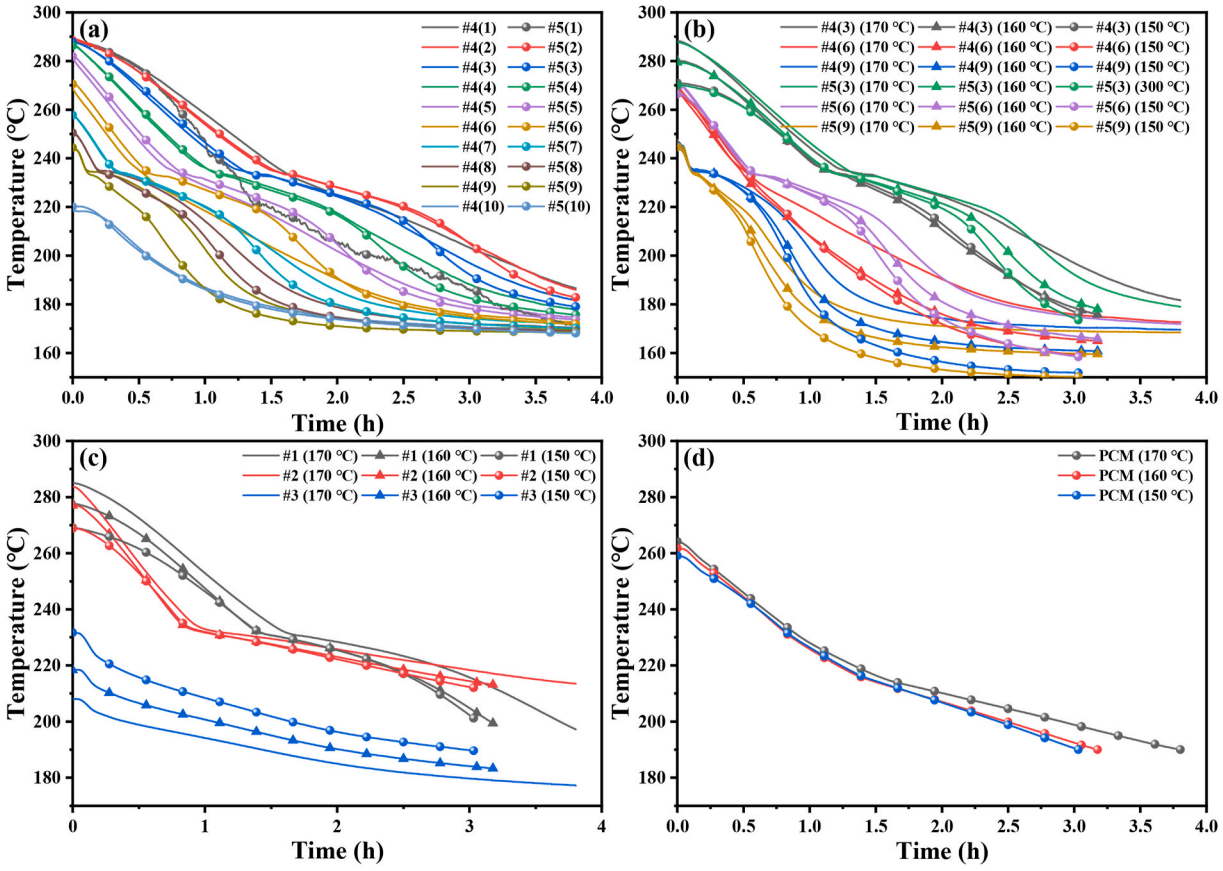

Fig. 12. Temperature evolution of (a) thermocouple sets #4 and #5 over time under the discharging temperature of 170 °C, and (b) thermocouples #4(3, 6, 9) and #5(3, 6, 9), (c) thermocouple sets #1, #2, and #3, (d) PCM over time under the charging temperatures of 170, 160, and 150 °C.

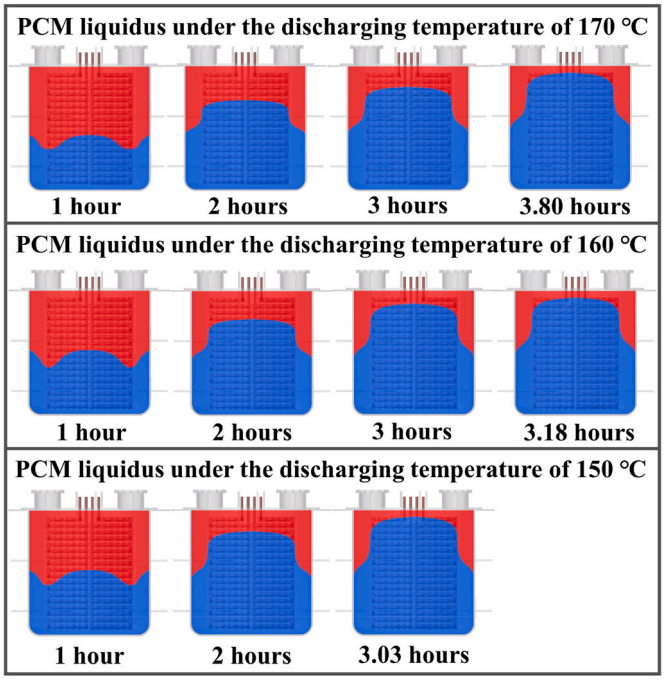

Fig. 13. Schematic diagrams of the PCM liquidus change under the discharging temperatures of 170, 160, and 150 °C.

(1) Increasing the charging HTF temperature could effectively shorten the charging duration, from 5.99 h at 280 °C to 4.54 h at 290 °C and 4.00 h at 300 °C, respectively, by 24.21% and 33.22%. While decreasing the discharging temperature resulted in a shorter discharging duration, from 3.80 h at 170 °C to 3.18 h at 160 °C and 3.03 h at 150 °C, respectively, by 16.32% and 20.26%. The impact of decreasing the discharging temperature on the charging/discharging duration was smaller than increasing the charging temperature due to the different heat transfer mechanisms of PCM during the charging and discharging processing.

(2) At the beginning of the charging process, the contribution of increasing the charging temperature to enhance heat transfer was limited due to the dominance of heat conduction. However, as charging progressed, natural convection caused by liquid PCM gradually dominated the heat transfer process, and increasing the charging temperature became more effective in enhancing heat transfer.

(3) During the discharging process, heat conduction dominated the heat transfer process as the PCM near the heat exchange tube gradually solidified. The heat transfer between HTF and PCM can only be achieved through heat conduction. Reducing the discharging temperature has a minor impact on enhancing heat transfer.

(4) Increasing the charging temperature from 280 to 290 and 300 °C could increase the average power of the LHS system from 45.2 to 58.12 and 67.62 kW, respectively, by 28.58% and 49.60%. While decreasing the discharging temperature from 170 to 160 and 150 °C improved the average power of the LHS system from 49.46 to 56.70 and 61.69 kW, respectively, by 14.64% and 24.73%. Increasing the charging temperature to enhance charging power

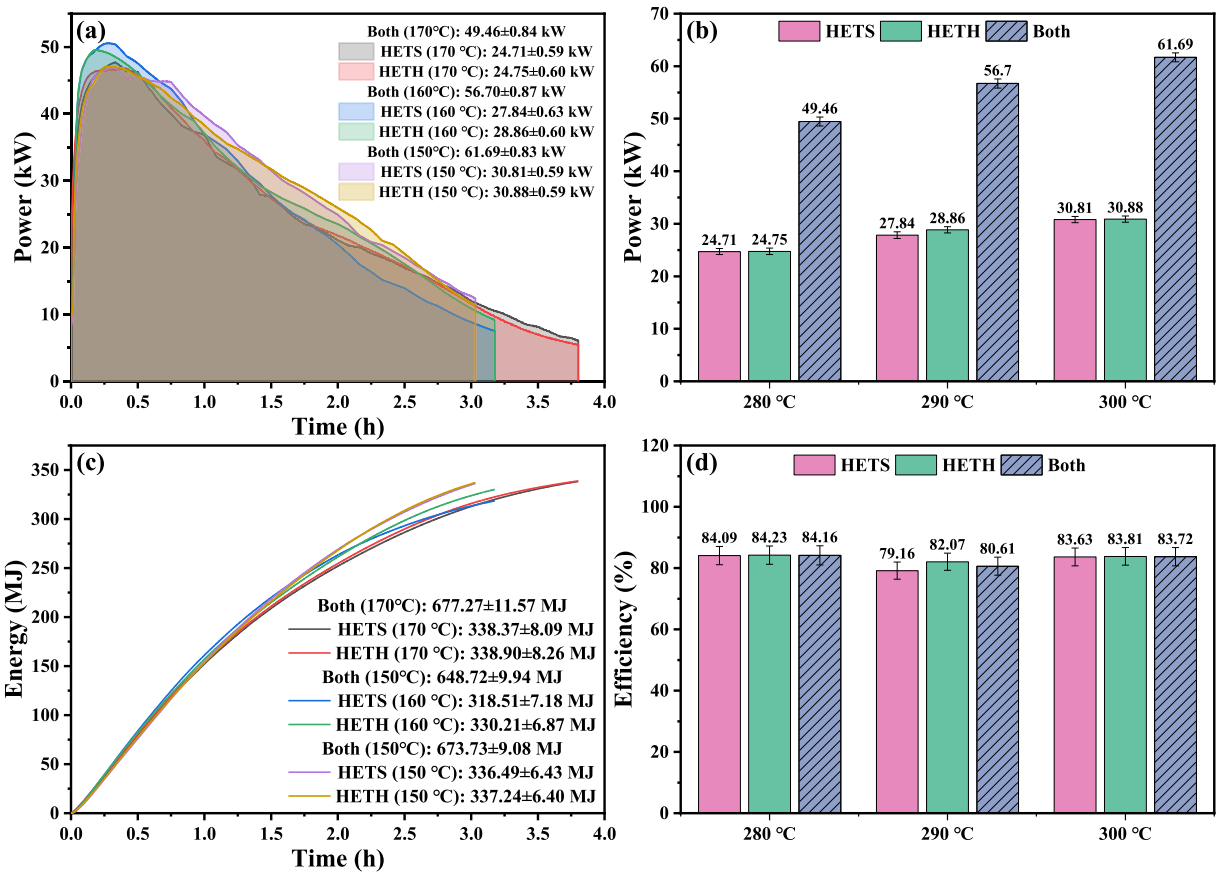

Fig. 14. (a) Instantaneous power curves, (b) average power of HETS, HETH, and both, (c) accumulative energy curves, and (d) charging efficiency of HETS, HETH, and both under the discharging temperatures of 170, 160, and 150 °C.

Table 4
Comparison of the critical parameters of the LHS systems for this work with those reported in previous studies.

PCM	Melting temperature of PCM (°C)	Stored energy (MJ)	Cycle efficiency (%)	Charging/discharging duration (h)	References
Dodecanoic acid	42.5	5	–	30/25	Murray and Groulx (2014)
Paraffin	44.32	26.28	91.8	5.8/13.3	Fadl and Eames (2019)
Sodium acetate trihydrate	59	4.3–6.3	–	1.9/1.9 (500 L/h)	Lin et al. (2020a)
Paraffin	61	0.043	95	3.5/2.8	Modi et al. (2023)
Paraffin/erythritol	59.4/118.8	51.3	63.4	8/9 (200 L/h)	Yang et al. (2023)
Molten salt	218–228	108	72	18.75/2.5	Zhang et al. (2016)
Sodium nitrate	305.1	19.5	–	4.9/5.6 (73 m^3/h)	Gurpreet Singh Sodhi and Muthukumar (2021)
Commercial nitrate	225.35	977.84	69.11	5.99/3.03 (280/150 °C)	This work
		952.37	68.33	4.54/3.18 (290/160 °C)	This work
		973.44	69.57	4.00/3.80 (300/170 °C)	This work

was more effective than increasing the discharging temperature to augment discharging power.

(5) The cycle efficiency of the LHS system in cases 1, 2, and 3 were 69.11%, 68.33%, and 69.57%, respectively, which suggested that the cycle efficiency of the system was independent of the charging and discharging temperature. The reasons for the low cycle efficiency were poor insulation performance and partially un-solidified PCM after discharging.

Based on the aforementioned conclusions, valuable guidance and practical insights can be derived. Firstly, due to natural convection, the temperature distribution of liquid PCM on the same horizontal plane is significantly more uniform than that of solid PCM. Secondly, increasing charging and discharging temperatures can effectively enhance their power outputs. However, increasing the charging temperature to enhance charging power is more effective, primarily due to variances in heat transfer mechanisms. Furthermore, a significant proportion of the lower cycle efficiency observed in the medium-temperature LHS systems is attributed to heat dissipation losses, which are considerably larger compared to low-temperature LHS systems. Therefore, insulation is imperative in practical applications. Lastly, cylindrical LHS systems exhibit a more uniform thermal stress distribution than cube LHS systems. However, this configuration may impede the efficient melting and solidification of PCM near the walls, leading to suboptimal PCM utilization. Thus, practical applications require further structural improvements.

CRediT authorship contribution statement

Laiquan Lv: Formal analysis, Investigation, Data curation, Writing – original draft, Project administration. **Shengyao Huang:** Visualization, Investigation. **Yang Zou:** Funding acquisition. **Xinyi Wang:** Funding acquisition. **Hao Zhou:** Conceptualization, Methodology, Validation.

Declaration of competing interest

The authors declare that they have no known competing financial interests or personal relationships that could have appeared to influence the work reported in this paper.

Data availability

Data will be made available on request.

Acknowledgments

This study was supported by the Fundamental Research Funds for the Central Universities (2022ZFJH004).

Appendix A. Supplementary data

Supplementary data to this article can be found online at https://doi.org/10.1016/j.jclepro.2023.138130.

References

Agyenim, Francis, Hewitt, Neil, Eames, Philip, Smyth, Mervyn, 2010. A review of materials, heat transfer and phase change problem formulation for latent heat thermal energy storage systems (LHTESS). Renew. Sustain. Energy Rev. 14, 615–628.
Al-abidi, Abduljalil A., Sohif Bin Mat, K. Sopian, Sulaiman, M.Y., Th Mohammed, Abdulrahman, 2013. CFD applications for latent heat thermal energy storage: a review. Renew. Sustain. Energy Rev. 20, 353–363.
Alem Kebede, Abraham, Kalogiannis, Theodoros, Van Mierlo, Joeri, Berecibar, Maitane, 2022. A comprehensive review of stationary energy storage devices for large scale renewable energy sources grid integration. Renew. Sustain. Energy Rev. 159.
Ammar, M., Abdulateef, Mat, Sohif, Abdulateef, Jasim, Sopian, Kamaruzzaman, Al-Abidi, Abduljalil A., 2018. Geometric and design parameters of fins employed for enhancing thermal energy storage systems: a review. Renew. Sustain. Energy Rev. 82, 1620–1635.
Avci, Mete, Yusuf Yazici, M., 2013. Experimental study of thermal energy storage characteristics of a paraffin in a horizontal tube-in-shell storage unit. Energy Convers. Manag. 73, 271–277.
Bourne, Stephen, Novoselac, Atila, 2016. Improved performance in tube-encapsulated phase change thermal energy stores for HVAC applications. Build. Environ. 98, 133–144.
Braxmeier, S., Hellmann, M., Beck, A., Umboock, A., Pluschke, G., Junghanss, T., Weinlaeder, H., 2009. Phase change material for thermotherapy of Buruli ulcer: modelling as an aid to implementation. J. Med. Eng. Technol. 33, 559–566.
Chavan, Santosh, Rudrapati, Ramesh, Manickam, Selvaraj, 2022. A comprehensive review on current advances of thermal energy storage and its applications. Alex. Eng. J. 61, 5455–5463.
Duan, Juan, Xiong, Yongliang, Yang, Dan, 2020. Study on the effect of multiple spiral fins for improved phase change process. Appl. Therm. Eng. 169.
Fadl, Mohamed, Eames, Philip C., 2019. An experimental investigation of the heat transfer and energy storage characteristics of a compact latent heat thermal energy storage system for domestic hot water applications. Energy 188.
Gurpreet Singh Sodhi, K. Vigneshwaran, Muthukumar, P., 2021. Experimental investigations of high-temperature shell and multi-tube latent heat storage system. Appl. Therm. Eng. 198.
Jahangir Khan, Rafid, Hossain Bhuiyan, Md Zubayer, Ahmed, Dewan Hasan, 2020. Investigation of heat transfer of a building wall in the presence of phase change material (PCM). Energy and Built Environment 1, 199–206.
Joybari, Mahmood Mastani, Seddegh, Saeid, Wang, Xiaolin, Haghighat, Fariborz, 2019. Experimental investigation of multiple tube heat transfer enhancement in a vertical cylindrical latent heat thermal energy storage system. Renew. Energy 140, 234–244.
Kalapala, Lokesh, Krishna Devanuri, Jaya, 2018. Influence of operational and design parameters on the performance of a PCM based heat exchanger for thermal energy storage – a review. J. Energy Storage 20, 497–519.
Khademi, Alireza, Shank, Kyle, Abtahi Mehrjardi, Seyed Ali, Tiari, Saeed, Sorrentino, Giancarlo, Said, Zafar, Chamkha, Ali J., Ushak, Svetlana, 2022. A brief review on different hybrid methods of enhancement within latent heat storage systems. J. Energy Storage 54.
Kline, S.J., Mcclintock, F.A., 1953. Describing Uncertainties in Single-Sample Experiments. Mechanical engineering, New York, N.Y., p. 75, 1919.
Lakshmi Narasimhan, N., 2019. Assessment of latent heat thermal storage systems operating with multiple phase change materials. J. Energy Storage 23, 442–455.
Li, Gang, 2015. Energy and exergy performance assessments for latent heat thermal energy storage systems. Renew. Sustain. Energy Rev. 51, 926–954.
Lin, Wenzhu, Zhang, Wenbo, Ling, Ziye, Fang, Xiaoming, Zhang, Zhengguo, 2020a. Experimental study of the thermal performance of a novel plate type heat exchanger with phase change material. Appl. Therm. Eng. 178.
Lin, Wenzhu, Ling, Ziye, Zhang, Zhengguo, Fang, Xiaoming, 2020b. Experimental and numerical investigation of sebacic acid/expanded graphite composite phase change material in a double-spiral coiled heat exchanger. J. Energy Storage 32.
Liu, Shuai, Peng, Hao, Hu, Zhiwei, Xiang, Ling, Huang, Jie, 2019. Solidification performance of a latent heat storage unit with innovative longitudinal triangular fins. Int. J. Heat Mass Tran. 138, 667–676.
Lv, Laiquan, Wang, Jiankang, Ji, Mengting, Zhang, Yize, Huang, Shengyao, Cen, Kefa, Zhou, Hao, 2022. Effect of structural characteristics and surface functional groups of biochar on thermal properties of different organic phase change materials: dominant encapsulation mechanisms. Renew. Energy 195, 1238–1252.
Lv, Laiquan, Zou, Yang, Huang, Shengyao, Wang, Xinyi, Shao, Rongyu, Xue, Xue, Yan, Rong, Zhou, Hao, 2023. Experimental study on a pilot-scale medium-temperature latent heat storage system with various fins. Renew. Energy 205, 499–508.
Mahdi, Jasim M., Lohrasbi, Sina, Nsofor, Emmanuel C., 2019. Hybrid heat transfer enhancement for latent-heat thermal energy storage systems: a review. Int. J. Heat Mass Tran. 137, 630–649.
Marian Diaconu, Bogdan, Cruceru, Mihai, Anghelescu, Lucica, 2023. A critical review on heat transfer enhancement techniques in latent heat storage systems based on phase change materials. Passive and active techniques, system designs and optimization. J. Energy Storage 61.
Modi, Nishant, Wang, Xiaolin, Negnevitsky, Michael, 2023. Experimental investigation of the effects of inclination, fin height, and perforation on the thermal performance of a longitudinal finned latent heat thermal energy storage. Energy 274.
Mosleh, Hassan Jafari, Ahmadi, Rouhollah, 2019. Linear parabolic trough solar power plant assisted with latent thermal energy storage system: a dynamic simulation. Appl. Therm. Eng. 161.
Mumah, S.N., 2008. Selection of heat storage materials for ammonia–water and lithium bromide solar-powered absorption heat pump systems. Int. J. Sustain. Energy 27, 81–93.
Murray, Robynne E., Groulx, Dominic, 2014. Experimental study of the phase change and energy characteristics inside a cylindrical latent heat energy storage system: Part 1 consecutive charging and discharging. Renew. Energy 62, 571–581.
Rajesh Baby, Balaji, C., 2012. Experimental investigations on phase change material based finned heat sinks for electronic equipment cooling. Int. J. Heat Mass Tran. 55, 1642–1649.
Shen, Yongliang, Mazhar, Abdur Rehman, Liu, Shuli, 2022. Comprehensive review on cascaded latent heat storage technology: recent advances and challenges. J. Energy Storage 55.
Sodhi, Gurpreet Singh, Jaiswal, Abhishek Kumar, Vigneshwaran, K., Muthukumar, P., 2019. Investigation of charging and discharging characteristics of a horizontal conical shell and tube latent thermal energy storage device. Energy Convers. Manag. 188, 381–397.
Tao, Y.B., He, Ya-Ling, 2018. A review of phase change material and performance enhancement method for latent heat storage system. Renew. Sustain. Energy Rev. 93, 245–259.
Waseem, Aftab, Ali, Usman, Shi, Jinming, Yuan, Kunjie, Qin, Mulin, Zou, Ruqiang, 2021. Phase change material-integrated latent heat storage systems for sustainable energy solutions. Energy Environ. Sci. 14, 4268–4291.
White, Martin T., Sayma, Abdulnaser I., 2020. A new method to identify the optimal temperature of latent-heat thermal-energy storage systems for power generation from waste heat. Int. J. Heat Mass Tran. 149.
Yang, Xiaohu, Guo, Junfei, Yang, Bo, Cheng, Haonan, Pan, Wei, He, Ya-Ling, 2020. Design of non-uniformly distributed annular fins for a shell-and-tube thermal energy storage unit. Appl. Energy 279.
Yang, Sheng, Shao, Xue-Feng, Luo, Jia-Hao, Oskouei, Seyedmohsen Baghaei, Bayer, Özgür, Fan, Li-Wu, 2023. A novel cascade latent heat thermal energy storage system consisting of erythritol and paraffin wax for deep recovery of medium-temperature industrial waste heat. Energy 265.
Zhang, P., Ma, F., Xiao, X., 2016. Thermal energy storage and retrieval characteristics of a molten-salt latent heat thermal energy storage system. Appl. Energy 173, 255–271.
Zhang, Chengbin, Li, Jie, Chen, Yongping, 2020. Improving the energy discharging performance of a latent heat storage (LHS) unit using fractal-tree-shaped fins. Appl. Energy 259.
Zhang, Yongxue, Lu, Bohui, Wang, Zixi, Zhu, Jianjun, Zhang, Jinya, Wang, Cong, 2022. Experimental investigation on the charging and discharging performance enhancement of a vertical latent heat thermal energy storage unit via snowflake fin design. Int. J. Heat Mass Tran. 199.
Zhou, Hao, Lv, Laiquan, Zhang, Yize, Ji, Mengting, Cen, Kefa, 2021. Preparation and characterization of a shape-stable xylitol/expanded graphite composite phase change material for thermal energy storage. Sol. Energy Mater. Sol. Cell. 230.
Zhou, Hao, Lv, Laiquan, Ji, Mengting, Zhang, Yize, Cheng, Fangzheng, Cen, Kefa, 2022. Experimental study of metal-oxide nanoparticles on the thermal properties of erythritol for thermal energy storage. Asia Pac. J. Chem. Eng. 17.